Available online at www.sciencedirect.com
ScienceDirect
Icarus 190 (2007) 423–431
ICARUS
www.elsevier.com/locate/icarus

The gas production of Comet 9P/Tempel 1 around the Deep Impact date ☆

M. Weiler [a,*], H. Rauer [a,b], J. Knollenberg [a], C. Sterken [c]

[a] *Institut für Planetenforschung, German Aerospace Center (DLR), Rutherfordstrasse 2, 12489 Berlin, Germany*
[b] *Zentrum für Astronomie und Astrophysik, Technische Universität Berlin, Germany*
[c] *Vrije Universiteit Brussel, Pleinlaan 2, 1050 Brussels, Belgium*

Received 5 May 2006; revised 27 December 2006

Available online 1 March 2007

Abstract

The target of the Deep Impact space mission (NASA), Comet 9P/Tempel 1, was observed from two nights before impact to eight nights after impact using the FORS spectrographs at the ESO VLT UT1 and UT2 telescopes. Low resolution optical long-slit spectra were obtained to study the evolution of the gas coma around the Deep Impact event. Following first results of this observing campaign on the CN and dust activity [Rauer, H., Weiler, M., Sterken, C., Jehin, E., Knollenberg, J., Hainaut, O., 2006. Astron. Astrophys. 459, 257–263], this work presents a study of the complete dataset on CN, C_2, C_3, and NH_2 activity of Comet 9P/Tempel 1. An extended impact gas cloud was observed moving radially outwards. No compositional differences between this impact cloud and the undisturbed coma were found as far as the observed radicals are concerned. The gas production rates before and well after impact indicate no change in the cometary activity on an intermediate time scale. Over the observing period, the activity of Comet 9P/Tempel 1 was found to be related to the rotation of the cometary nucleus. The rotational lightcurve for different gaseous species provides indications for compositional differences among different parts of the nucleus surface.

Keywords: Comets; Comet Tempel-1

1. Introduction

On July 4, 2005, at 05:52:02 UT ground received time (A'Hearn et al., 2005), the NASA Deep Impact mission delivered an impactor of 370 kg mass into the nucleus of the Jupiter family Comet 9P/Tempel 1. During this event, a kinetic energy of 19.3 GJ was released, causing the formation of a crater and the ejection of a cloud of debris (A'Hearn et al., 2005). Comet 9P/Tempel 1 was observed around this Deep Impact event by a global observing campaign (Meech et al., 2005), including the European Southern Observatory (ESO) with its seven telescopes located in Chile. One scientific program executed at ESO was the study of the gas coma before and after the impact event by means of low resolution optical long-slit spectroscopy. Although Comet 9P/Tempel 1 was below the horizon at the time of impact, it could be observed up to approximately two hours before the impact and again approximately 18 h after, for roughly four hours per night. The observations open the opportunity to quantitatively study the most abundant radicals in the cometary coma, CN, C_2, C_3, and NH_2. This allows us to answer questions about the mass of the impact ejecta cloud, if the cloud was compositionally different compared to the undisturbed coma, and whether the activity of Comet 9P/Tempel 1 was significantly modified due to the impact. First results of this observing campaign on the CN and dust activity are described by Rauer et al. (2006). Here, we extend this study and include other radicals observed as well as additional slit orientations to study anisotropy in the coma.

2. Observations and data reduction

The observing program used the VLT UT1 telescope and the FORS2 spectrograph and the VLT UT2 telescope with the FORS1 spectrograph. The observing period covered two nights before and eight nights following the impact event. An observ-

☆ Based on observations collected at the European Southern Observatory, Chile (ESO Progamme 075.C-0355).

* Corresponding author. Fax: +49 30 67055 384.
E-mail address: mich.weiler@googlemail.com (M. Weiler).

0019-1035/$ – see front matter
doi:10.1016/j.icarus.2007.01.015

Table 1
Overview of the instrument parameters used for the observations

Instrument	Slit length	Slit width	Pixel size	Δλ
FORS1	6.8′	1″	0.200″/pixel	1.20 Å/pixel
FORS2	6.8′	1″	0.252″/pixel	1.50 Å/pixel

Note. Δλ gives the wavelength increment.

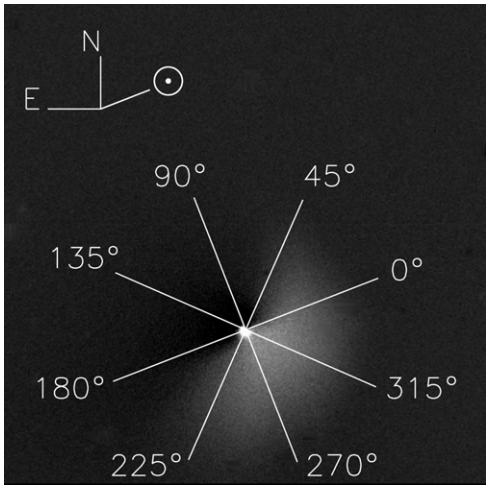

Fig. 1. Difference of *R*-filter images before and after impact. The impact dust cloud can be seen to the southwest. The field of view is 1.3′, corresponding to 4.94×10^4 km. The slit orientations discussed in the text are indicated by lines. Stars in the field of view were removed by interpolation from the neighboring pixels. The projected solar direction is indicated.

ing window of approximately four hours per night was available for comet observations. A complete overview of this observing program is given by Rauer et al. (2006), including a full observing log. The data reduction applied to the spectra is also described therein.

In the nights from July 2 to July 10, the FORS2 instrument was used. In the two additional nights from July 10 to July 12, spectra with the FORS1 instrument were taken. The instrument characteristics are summarized in Table 1. A slit with 1 arcsec width and 6.8 arcmin length was centered on the optocenter of the cometary coma. Four different position angles were used to obtain not only a radial but also azimuthal information within the coma. The position angles with respect to the projected solar direction (within 291.7° to 290.5° in the equatorial reference frame) are 0°–180°, 45°–225°, 90°–270°, and 135°–315°. Fig. 1 shows Comet Tempel 1 taken in *R* band 17^h32^m after impact, after subtraction of the pre-impact coma. The slit orientations are indicated, a dust cloud produced by the impact can be seen towards the southwest. The spectra obtained within the observing program cover the wavelength region from 3700 to 6200 Å. At least one spectrum along the 0°–180° direction was taken each night covering the wavelength range from 6100 to 9200 Å. But since all strong gaseous emissions in the cometary coma are located at wavelengths shorter than 6200 Å, only the spectra taken in the first wavelength region are analyzed within this work.

Fig. 2 shows a pre-impact and a post-impact spectrum of Comet 9P/Tempel 1 after subtraction of the continuum caused

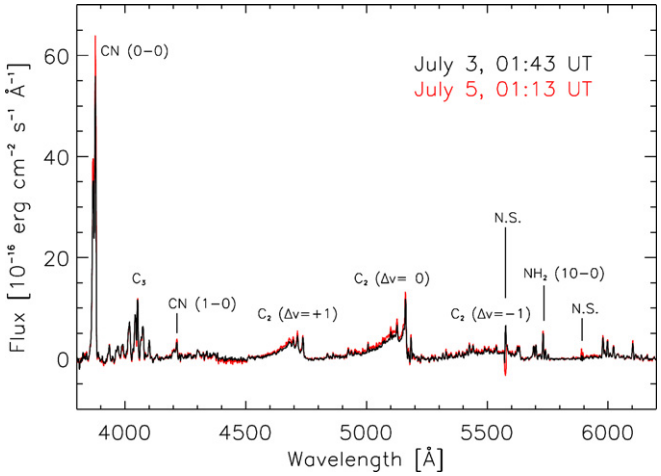

Fig. 2. Spectra of Comet 9P/Tempel 1, obtained by integrating from the nucleus position to 1.5×10^4 km projected nucleocentric distance in the 315° direction. The continuum is subtracted. A pre-impact spectrum (black) and a post-impact spectrum (red), showing a slight enhancement in the gas emissions, are presented. Remnants of night ska lines are marked with N.S. (For interpretation of the references to color in this figure legend, the reader is referred to the web version of this article.)

by scattering of sunlight by dust particles. The strong emissions originating from the CN, C_2, C_3, and NH_2 radicals were clearly detected. In this work, the CN (0–0) emission, the C_3 emission, the C_2 ($\Delta v = 0$) emission, and the NH_2 (10–0) emission are analyzed quantitatively.

3. Impact cloud kinetics

When comparing the radial emission profiles of the nights following on the impact event with the ones obtained during the two nights before the impact, an extended cloud of gas released by the impact can be identified. This cloud is especially prominent in the CN and C_2 emissions, providing a good signal to noise ratio, and can also be identified in the emissions of C_3 and NH_2, although with low signal-to-noise ratio. The cloud can be observed at all position angles used, thus it moved all around the nucleus. With time, a radial expansion of the cloud can be observed. Fig. 3 shows the radial emission profiles of the CN violet system along the 0°–180° direction on the night of July 04/05, after subtraction of the mean profile of the night before. The impact cloud on both sides of the nucleus and its movement within the night can be seen. The gas cloud can be observed for four nights after impact. Then, all gas emissions are back to the pre-impact level.

For the night of July 04/05, the entire cloud lies within the field-of-view of the slit and thus, the radial expansion velocity of the outermost part of the cloud can be determined from its position in spectra taken at different times within that night. This was done by comparing a post-impact radial emission profile with the pre-impact emission profile and determining the radial position inside which the profiles differ. The errors were estimated from determining the positions at which the radial emission profiles are clearly in agreement and disagreement, respectively. Fig. 4 shows the first post-impact radial emission profile for CN taken in the 180° direction, together with the

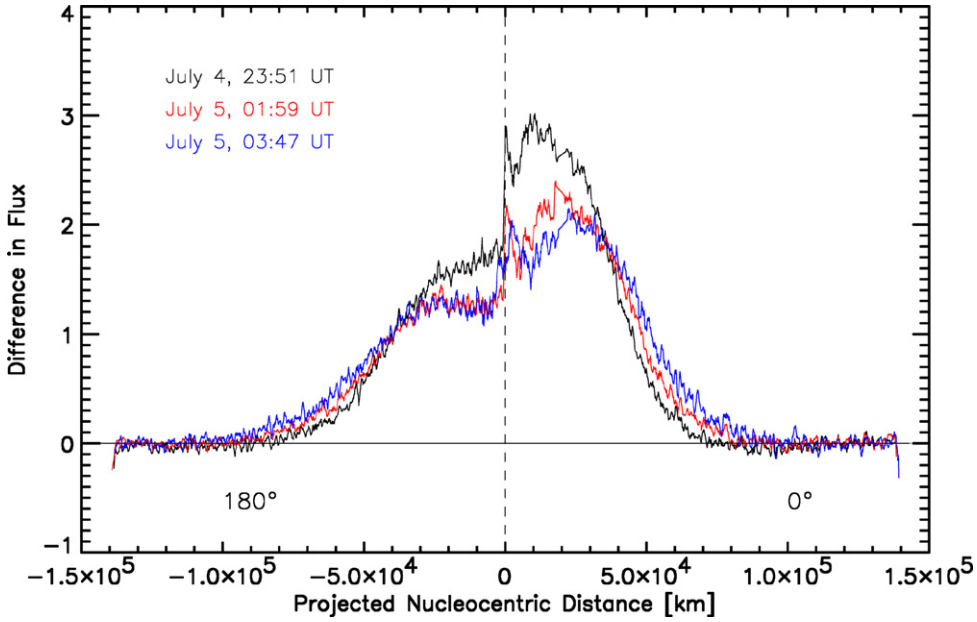

Fig. 3. The CN impact cloud. The radial CN flux profiles obtained in the 0°–180° direction during the night July 04/05 are shown. The mean radial intensity profile from the night July 03/04 is subtracted and the resulting profiles were smoothed over a range of 5 pixels. At projected nucleocentric distances from 0 km to about 10^4 km, an increase in the CN flux profile can be seen, moving away from the nucleus position with time. The difference in flux is given in 10^{-16} erg s^{-1} cm^{-2}.

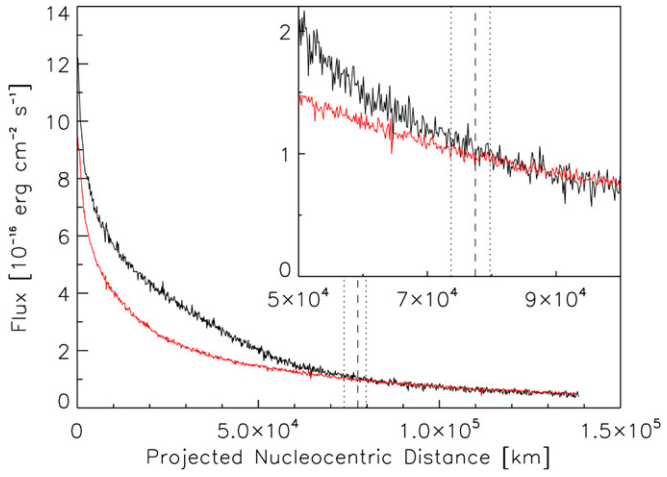

Fig. 4. Mean radial CN emission profile of the night July 03/04 in the 180° direction (red), compared with the first CN emission profile in the same direction obtained after impact. The estimated position of the outermost detectable part of the CN cloud is indicated by a dashed line, while the estimated uncertainties are indicated by dotted lines. The insert in the upper right corner shows a detail of the larger diagram. (For interpretation of the references to color in this figure legend, the reader is referred to the web version of this article.)

mean CN profile along this direction from the night of July 03/04. The estimated position of the outermost detectable part of the CN cloud is indicated, together with the estimated uncertainties. Since this method cannot take into account slight offsets between the two emission profiles due to uncertainties in the photometric calibration or the continuum subtraction, the true errors may be somewhat larger than the estimated ones.

Table 2 summarizes the positions of the outermost detectable part of the CN and C_2 cloud at different times, together with the projected mean gas expansion velocities derived. The velocities were computed by dividing the position of the outermost detectable part of the gas cloud by the time since impact. No significant difference in projected mean velocities between the

Table 2
Determination of the projected velocities of the outermost detectable part of the impact cloud

p.a.	T [s]	CN		C_2	
		x [10^3 km]	v [km s^{-1}]	x [10^3 km]	v [km s^{-1}]
0°	65,182	$75.0^{+2.5}_{-2.5}$	$1.15^{+0.04}_{-0.04}$	$76.3^{+1.1}_{-1.6}$	$1.17^{+0.02}_{-0.03}$
	72,861	$84.5^{+2.5}_{-5.7}$	$1.16^{+0.03}_{-0.08}$	$75.2^{+1.6}_{-1.6}$	$1.03^{+0.02}_{-0.02}$
	79,334	$88.3^{+6.2}_{-2.1}$	$1.11^{+0.08}_{-0.03}$	$80.6^{+3.3}_{-2.6}$	$1.02^{+0.04}_{-0.02}$
45°	71,514	$105.8^{+5.7}_{-3.3}$	$1.48^{+0.08}_{-0.05}$	$72.7^{+11.2}_{-5.7}$	$1.02^{+0.16}_{-0.08}$
90°	68,628	$77.8^{+3.3}_{-1.5}$	$1.15^{+0.05}_{-0.02}$	$102.1^{+3.8}_{-14.3}$	$1.49^{+0.06}_{-0.21}$
135°	70,143	$80.1^{+15.3}_{-6.6}$	$1.14^{+0.22}_{-0.09}$	$83.7^{+3.3}_{-4.9}$	$1.19^{+0.05}_{-0.07}$
	74,302	$87.4^{+7.5}_{-8.2}$	$1.18^{+0.10}_{-0.11}$	$81.2^{+8.2}_{-4.1}$	$1.09^{+0.11}_{-0.06}$
	77,882	$93.4^{+7.7}_{-4.9}$	$1.20^{+0.10}_{-0.06}$	$80.9^{+8.5}_{-4.6}$	$1.04^{+0.11}_{-0.06}$
180°	65,182	$77.5^{+2.3}_{-3.8}$	$1.19^{+0.04}_{-0.06}$	$83.7^{+1.6}_{-1.6}$	$1.28^{+0.03}_{-0.03}$
	72,861	$88.6^{+5.1}_{-3.8}$	$1.22^{+0.07}_{-0.05}$	$83.0^{+4.4}_{-1.5}$	$1.14^{+0.06}_{-0.02}$
	79,334	$99.0^{+1.8}_{-3.9}$	$1.25^{+0.02}_{-0.05}$	$89.6^{+8.0}_{-3.6}$	$1.13^{+0.10}_{-0.05}$
225°	71,514	$89.9^{+1.0}_{-4.8}$	$1.16^{+0.01}_{-0.07}$	$86.2^{+1.1}_{-4.1}$	$1.20^{+0.02}_{-0.06}$
270°	68,628	Bad column		$82.9^{+3.6}_{-2.5}$	$1.21^{+0.05}_{-0.04}$
315°	70,143	$80.7^{+3.4}_{-2.8}$	$1.15^{+0.05}_{-0.04}$	$82.1^{+1.6}_{-1.6}$	$1.17^{+0.02}_{-0.02}$
	74,302	$88.1^{+6.2}_{-4.4}$	$1.19^{+0.08}_{-0.06}$	$79.6^{+3.3}_{-3.3}$	$1.07^{+0.04}_{-0.04}$
	77,882	$89.4^{+18.9}_{-4.4}$	$1.15^{+0.24}_{-0.06}$	$82.5^{+3.9}_{-4.3}$	$1.06^{+0.05}_{-0.06}$
Mean			1.23 ± 0.12		1.17 ± 0.14

Note. T gives the time since impact and x the radial position of the outermost detectable part of the impact ejecta cloud.

two species were found. Since the position of the C_3 and NH_2 clouds cannot be measured with sufficient accuracy for this purpose, these species were not used for the determination of gas expansion velocities.

Furthermore, the projected velocity of the center of the CN and C_2 clouds were determined. Therefore, the geometric dilution of the cloud when expanding outwards from the nucleus has to be considered. In the case of a steady-state outflow from the nucleus with constant velocity, the observed column density decreases with the projected nucleocentric distance r as r^{-1}. However, in the case of the Deep Impact event, a transient expansion of an isolated cloud in the coma has to be regarded. In this case, the gas released by the impact event can be assumed to expand in radial and lateral direction while the cloud as a whole is moving outwards from the nucleus with a constant velocity. For the lateral expansion, two extreme cases are regarded in the following. First, it is assumed that the cloud moves all around the nucleus, forming a shell-like structure. Second, it is assumed that the cloud is filling the same solid angle as seen from the nucleus at all times and that it is having a spherical shape. The radial expansion in the two cases is then given by the increase of the thickness of the shell or the diameter of the sphere, respectively. For a sphere, its diameter has to increase linearly with increasing nucleocentric distance to ensure that it fills a constant solid angle. It is assumed that the thickness of the shell is also increasing linearly with nucleocentric distance. Since the detailed distribution of gas in the cloud is not known, a homogeneous density inside the cloud is assumed. What is accessible to observations is the column density in the cloud only. In the extreme cases regarded here, the maximum value of the column densities inside the cloud decreases with r^{-2} while the cloud is moving outwards from the nucleus. Although the described model is strongly simplified, a decrease of the column density according to r^{-2} instead of the usual assumption according to r^{-1} appears as a more realistic choice for the Deep Impact event. Therefore, the flux value measured at a certain distance to the nucleus position was multiplied with the square of its distance to the nucleus in order to correct for the geometric dilution.

A Gaussian profile was then fitted to the inner part of the distance-corrected cloud and the resulting position of the center of the Gaussian was assumed to be the position of the center of the gas cloud. This method was applied to the CN and C_2 profiles. For C_3 and NH_2 the signal to noise was not sufficient to obtain a reliable Gaussian fit. The resulting velocities of the center of the CN and C_2 clouds are presented in Table 3.

The interpretation of the derived values for the velocities of the outermost detectable parts of the gas clouds and for their centers is difficult. The observed emission profiles are influenced not only by the movement of material but also by the formation mechanisms of the observed radicals. They are not producted by the impact event but as a function of time by the decay of parent species released by the impact event. During formation, the radicals may receive an excess energy that results in a higher velocity of the radicals compared to their parent species. Since the additional velocity associated with the excess energy is random distributed in their direction, the observed cloud of radicals can be expected to be broader than the corresponding cloud of the parent species.

Table 3
Determination of the projected gas bulk velocities

p.a.	T [s]	CN		C_2	
		x [10^3 km]	v [km s^{-1}]	x [10^3 km]	v [km s^{-1}]
0°	65,182	37.5 ± 3.0	0.58 ± 0.05	44.7 ± 5.3	0.69 ± 0.08
	72,861	43.5 ± 3.2	0.60 ± 0.04	47.6 ± 4.8	0.65 ± 0.07
	79,334	47.8 ± 3.2	0.60 ± 0.04	54.9 ± 4.7	0.69 ± 0.06
45°	71,514	46.3 ± 3.0	0.65 ± 0.04	54.4 ± 4.6	0.76 ± 0.07
90°	68,628	39.5 ± 3.7	0.58 ± 0.05	55.2 ± 6.0	0.80 ± 0.09
135°	70,143	42.6 ± 3.2	0.61 ± 0.05	54.6 ± 4.9	0.78 ± 0.07
	74,302	43.9 ± 3.1	0.59 ± 0.04	55.6 ± 4.7	0.75 ± 0.06
	77,882	47.1 ± 3.1	0.60 ± 0.04	55.3 ± 4.1	0.71 ± 0.05
180°	65,182	41.3 ± 3.0	0.63 ± 0.05	50.9 ± 5.1	0.78 ± 0.08
	72,861	46.2 ± 3.0	0.63 ± 0.04	51.8 ± 4.3	0.71 ± 0.06
	79,334	50.4 ± 3.0	0.64 ± 0.04	58.3 ± 4.3	0.73 ± 0.05
225°	71,514	46.9 ± 3.0	0.66 ± 0.04	54.6 ± 4.4	0.76 ± 0.06
270°	68,628	49.1 ± 3.1	0.72 ± 0.05	54.0 ± 5.6	0.79 ± 0.08
315°	70,143	46.3 ± 3.4	0.66 ± 0.05	51.4 ± 4.0	0.73 ± 0.06
	74,302	48.9 ± 3.2	0.66 ± 0.04	54.8 ± 7.1	0.74 ± 0.10
	77,882	49.6 ± 3.1	0.64 ± 0.04	55.6 ± 5.8	0.71 ± 0.07
Mean			0.63 ± 0.04		0.75 ± 0.04

Note. T gives the time since impact and x the radial position of the center of the impact ejecta cloud.

The CN parent Haser scale length is shorter and the daughter scale length is longer than the corresponding values for C_2, as shown in Section 4. Therefore, the observed CN radicals in the cloud may be produced earlier than the observed C_2 radicals. Due to the excess velocity, the outermost detectable CN radicals could have reached larger distances than the C_2 radicals within the same time. The position of the center of the CN cloud and the C_2 cloud however is likely to be unaffected by this effect due to the random distribution of the excess velocity vectors. Therefore, one would expect the velocity of the outermost detectable part of the CN cloud to be higher than for the C_2 cloud, while the velocities of the center of the CN and C_2 clouds are similar. However, the opposite effect is observed, and the velocities of the outermost parts of the clouds are similar while the center of the C_2 cloud moved faster than the center of the CN cloud. This remains unexplained by the strongly simplified model used in this work and may has its reason in the detailed dynamics and chemistry in the impact cloud.

4. Gas production rates

In order to study the effects of the impact event on an intermediate time scale, the Haser production rates for the species CN, C_2, C_3, and NH_2 were determined in the two nights before impact and in the fifth and sixth night (July 08/09 and 09/10) after impact, when the coma was obviously back to its pre-impact state. In order to estimate the influence of asymmetry of the coma on the determination of the production rates, the radial intensity profiles at four different position angles available

Table 4
Summary of the Haser parent (l_p) and daughter (l_d) scale lengths determined from the observations of Comet 9P/Tempel 1

Species	July 02/03	July 03/04	July 08/09	July 09/10
CN	$l_p = 1.73 \pm 0.69$	$l_p = 2.00 \pm 0.45$	$l_p = 2.43 \pm 0.44$	$l_p = 2.04 \pm 0.52$
	$l_d = 54.67 \pm 41.00$	–	–	–
C_2	$l_p = 4.58 \pm 1.34$	$l_p = 4.13 \pm 0.83$	$l_p = 4.87 \pm 0.59$	$l_p = 3.93 \pm 0.30$
	$l_d = 4.58 \pm 1.34$	$l_d = 5.80 \pm 2.34$	$l_d = 5.49 \pm 0.85$	$l_d = 4.48 \pm 0.82$
C_3	$l_p = 0.33 \pm 0.04$	$l_p = 0.31 \pm 0.06$	–	–
	$l_d = 9.79 \pm 6.26$	$l_d = 17.06 \pm 5.95$	–	–
NH_2	$l_p = 1.34 \pm 0.28$	$l_p = 1.20 \pm 0.51$	$l_p = 1.28 \pm 0.22$	$l_p = 1.93 \pm 0.56$
	$l_d = 1.51 \pm 0.52$	$l_d = 1.37 \pm 0.49$	$l_d = 1.36 \pm 0.31$	$l_d = 1.93 \pm 0.56$

Note. The scale lengths were extrapolated to a heliocentric distance of 1.0 AU by assuming a scaling with r_h^2. All values are given in [10^4 km].

for all pre-impact observing nights (0°, 90°, 180°, and 270°) were used independently. The Haser parent and daughter scale lengths and the production rates were fitted to the radial column density profiles simultaneously. The resulting scale lengths are summarized in Table 4. Since the CN daughter scale length is quite large, it could only be determined in the night of July 02/03, where the comet was placed close to the edge of the long-slit in some exposures. The derived CN daughter scale length was then used for the computation of the CN production rates in all nights. The C_3 scale lengths could only be determined if at least four spectra (of the same slit orientation) were co-added to increase the signal-to-noise ratio. This was only possible in the nights of July 02/03 and July 03/04. The derived scale lengths also gave a good fit of the radial intensity profiles in all other nights.

The values for the parent and daughter scale lengths of CN, C_3, and C_2 are in agreement with the corresponding scale lengths derived from observations of other comets (Rauer et al., 2003 and references therein). The parent scale lengths of NH_2 derived in this work are roughly by a factor 2–3 larger than the values published for other comets (Rauer et al., 2003). Using the photodissociation rate coefficient of NH_3 for the formation of NH_2 of 1.7×10^4 s^{-1} (Huebner et al., 1992) and assuming the gas velocity of 1 km s^{-1}, a NH_2 parent scale length of 5.9×10^3 km would be expected if NH_3 is the dominant NH_2 parent species, which is not in agreement with the result obtained in this work. The NH_2 daughter scale lengths are in agreement with values presented in other publications, ranging from $6.9 \pm 2.0 \times 10^3$ km (Fink et al., 1991) to 6.2×10^4 km (Cochran et al., 1992).

The *g*-factors applied for the conversions from observed emission line fluxes to column densities where taken from Schleicher (1983) (CN), Cochran et al. (1992) (C_3 and C_2), and Kawakita and Watanabe (2002) (NH_2). A mean nucleus radius for Comet Tempel 1 of 3.0 km (A'Hearn et al., 2005) was assumed. In order to be comparable with other publications, the often assumed gas expansion velocity of 1 km s^{-1} for the parent and daughter species was used for the determination of the gas production rates. The excess velocities of daughter species are not taken into account since their values are highly uncertain and the assumption of some value might complicate the comparison of the production rates derived in this work with values from other publications. The production rates are presented in Table 5. The production rates were determined for each spectrum and each particular position angle independently. The uncertainty resulting from the continuum subtraction was used for the weighting of each radial data point in each emission profile. Based on these results, a single production rate with an uncertainty resulting from the fitting was obtained. If more than one spectrum at a particular position angle was obtained during one night, the resulting production rates were averaged and the uncertainties of each single spectrum were taken into account. This procedure allows to take the uncertainty resulting from variations between different spectra of one night (e.g., due to improper extinction correction or variations in the sky transmission) into account. In cases where only one spectrum for a particular position angle was obtained within a night, the error in the production rate listed in Table 5 only includes the

Table 5
Summary of the Haser production rates determined from the observations of Comet 9P/Tempel 1

Species	p.a.	July 02/03	July 03/04	July 08/09	July 09/10
CN	0°	10.8 ± 0.4	13.7 ± 0.4.	15.8 ± 2.9	12.8 ± 1.3
	90°	7.3 ± 0.3	8.2 ± 0.2	9.7 ± 0.5	8.1 ± 0.1
	180°	8.4 ± 0.9	8.1 ± 0.3	10.2 ± 0.3	9.1 ± 0.3
	270°	16.6 ± 0.8	13.2 ± 0.3	15.8 ± 0.6	15.4 ± 0.5
CN	Mean	10.2 ± 2.6	10.8 ± 3.1	12.9 ± 3.4	11.4 ± 3.4
C_2	0°	19.6 ± 1.6	19.7 ± 1.1	18.5 ± 0.9	14.7 ± 4.0
	90°	14.7 ± 0.1	12.0 ± 4.8	17.2 ± 2.8	13.4 ± 0.3
	180°	14.7 ± 0.7	10.9 ± 3.1	15.0 ± 1.0	12.7 ± 1.2
	270°	24.4 ± 0.6	15.5 ± 4.5	14.8 ± 4.5	15.7 ± 0.6
C_2	Mean	18.4 ± 4.6	14.5 ± 4.0	16.4 ± 1.8	14.1 ± 1.3
C_3	0°	2.2 ± 0.1	1.8 ± 0.1	1.8 ± 0.2	1.8 ± 0.1
	90°	1.8 ± 0.1	1.3 ± 0.1	1.8 ± 0.1	1.5 ± 0.1
	180°	1.2 ± 0.2	1.1 ± 0.1	1.1 ± 0.3	1.1 ± 0.2
	270°	1.8 ± 0.1	1.6 ± 0.2	1.8 ± 0.2	1.4 ± 0.2
C_3	Mean	1.7 ± 0.4	1.4 ± 0.3	1.6 ± 0.4	1.4 ± 0.3
NH_2	0°	10.3 ± 1.7	11.2 ± 2.5	10.4 ± 1.1	10.9 ± 1.1
	90°	8.6 ± 0.3	6.9 ± 0.8	7.3 ± 0.4	10.7 ± 20.7
	180°	7.2 ± 4.8	5.1 ± 0.8	5.9 ± 0.5	10.1 ± 6.9
	270°	7.5 ± 0.7	5.6 ± 1.9	7.6 ± 0.8	6.5 ± 0.1
NH_2	Mean	8.4 ± 1.4	7.2 ± 2.8	7.8 ± 1.9	9.6 ± 2.0

Note. The row with 'mean' as the position angle (p.a.) gives the production rate averaged over all four p.a. All numbers are expressed in [10^{24} s^{-1}].

Table 6
The number of radicals in the impact cloud as determined at different times, and the derived number of parent molecules released by the impact event

T [s]	p.a.	CN	CN parent	C_2	C_2 parent	C_3	C_3 parent
65,182	0°	3.27 ± 0.47	4.63 ± 0.73	1.92 ± 0.30	5.27 ± 1.26	0.82 ± 0.09	1.04 ± 0.26
	180°	2.33 ± 0.35	2.75 ± 0.43	1.62 ± 0.23	3.28 ± 0.90	0.28 ± 0.07	0.33 ± 0.13
68,628	90°	2.70 ± 0.50	3.27 ± 0.62	2.51 ± 0.31	6.71 ± 2.06	0.21 ± 0.04	0.28 ± 0.05
	270°	2.40 ± 0.35	2.90 ± 0.44	2.01 ± 0.26	5.61 ± 1.55	0.43 ± 0.04	0.51 ± 0.07
72,861	0°	3.38 ± 0.66	4.57 ± 0.94	1.71 ± 0.41	4.48 ± 1.38	1.37 ± 0.12	1.79 ± 0.49
	180°	2.50 ± 0.48	2.88 ± 0.57	1.39 ± 0.30	2.72 ± 0.87	0.53 ± 0.09	0.63 ± 0.24
79,334	0°	3.88 ± 0.68	5.09 ± 0.94	2.44 ± 0.44	6.21 ± 1.68	0.93 ± 0.13	1.25 ± 0.40
	180°	2.95 ± 0.49	3.36 ± 0.58	1.84 ± 0.33	3.52 ± 1.05	<0.12	<0.15

Note. All numbers mean 10^{29} molecules. T gives the time since impact and the position angle (p.a.) with respect to the solar direction.

uncertainty resulting from the fit of the Haser model to the radial emission profile. In this cases, the error specified in Table 5 might be underestimated. For the computation of the mean production rates of the species CN, C_2, C_3, and NH_2 in Table 5, no weighting with the errors of the results obtained for the four different position angles was therefore applied.
The derived mean gas production rates show no significant change after five days after impact compared to the pre-impact activity.

5. Quantitative study of the impact cloud

Since the detailed dynamics of the impact cloud is not known, the abundances of the parent species can only be determined when treating the cloud as a whole. If the total number of daughter radicals in the impact cloud can be determined, i.e., as long as the whole cloud is covered by the long-slit, and if it is assumed that all material that lead to formation of the cloud was released at the same time, a two-step chemical model for the production and destruction of the observed daughter species can be applied without using the information on the radial distribution of the daughter radicals. A description of this approach is given by Rauer et al. (2006). The number of parent molecules, N_p, released by the impact is then related to the number of their daughter radicals, N_d, in the cloud observed at a time T after impact:

$$N_p = N_d(T)\left(\frac{k_p}{k_d - k_p}\left[e^{-k_p T} - e^{-k_d T}\right]\right)^{-1}. \quad (1)$$

The values for the rate coefficients k_p and k_d can be derived from the ratio of the gas velocity and the parent and daughter scale lengths, respectively. For the scale lengths, the values derived from the observations on July 03/04 were used. This approach assumes that the formation mechanisms of the radicals in the impact cloud are the same than in the undisturbed pre-impact coma. The mean velocity values given in Table 2 were used for CN and C_2. For C_3, a velocity of 1.2 km s^{-1} was assumed. The total number of daughter radicals within the gas cloud is determined by integrating over the difference between the emission profiles obtained in the night of July 04/05 and the mean emission profile from the previous night. This approach makes the assumption that all differences between the night of July 03/04 and July 04/05 are a result of the impact event. For each profile, a rotational symmetry was assumed to determine the number of radicals in the impact cloud. The number of radicals in the impact cloud determined that way are listed in Table 6 for CN, C_2, and C_3. Due to the low signal-to-noise ratio of the NH_2 emission, no useful results for NH_2 could be obtained. Differences between the results from profiles taken at different position angles are caused by the asymmetry of the cloud. This effect is not included in the error bars. The number of parent molecules derived from the total number of radicals by using Eq. (1) are also listed in Table 6.

As discussed by Rauer et al. (2006), the amount of volatiles released due to the impact requires the injection of icy grains into the coma by the Deep Impact event. The energy provided by the impact event is not sufficient to sublimate the observed amount of volatiles. These icy grains than produce a significant part of the observed gas cloud by sublimation caused by solar irradiation. A detailed discussion of the assumptions made here can be found at Rauer et al. (2006).

6. Comparison of the coma and the impact cloud composition

In order to compare the chemical composition of the coma before impact, after impact, and the composition of the impact gas cloud, the ratios of the Haser production rates for C_2/CN and C_3/CN were computed. Furthermore, the number of the parent molecules for C_2, C_3, and CN as computed for the impact cloud can be used to determine the ratio of the parents in the cloud. Since the simple chemical model is the same for the two cases, the results are comparable. The ratios of the two nights before impact and the two nights after impact were averaged. The abundance ratios are given in Table 7 for the different slit orientations and the corresponding average. Since the production rates and the number of parent molecules determined in different directions from the nucleus do not represent direct measurements of the mean value averaged over the entire coma, the corresponding average values were computed as the unweighted means.

The ratio of C_2/CN makes Comet 9P/Tempel 1 typical according to A'Hearn et al. (1995), in agreement with previous observations (e.g., Cochran et al., 1992). The large uncertainty in the ratio of C_3/CN is caused by the low signal to noise ratio of the C_3 emission.

It can be seen that the mean composition of the impact cloud as obtained with the Haser model is identical to the pre-impact coma, as far as C_2, C_3, and CN are concerned. A slightly lower value for C_2/CN after impact is found. This is mainly caused by a low C_2 production rate in the 270° direction.

7. Rotational coma variations

Short-term variations in the radial emission profiles suggest to search for variations with the rotational period of the comet nucleus. Such a short-term variation can be seen in Fig. 3, where an apparently new peak occurred in the radial intensity profile within about 6000 km on the sunward side of the nucleus, moving outwards with time. To study short-term variability, the flux in the inner part of the coma is integrated in single spectra and plotted versus the rotational phase of the nucleus. The inner seven pixels in the coma, corresponding to 1.8 arcsec, were excluded for integration due to difficulties with the continuum subtraction. Then, the flux within the following 20 pixels, corresponding to 5 arcsec, were integrated on both sides from the nucleus. This small aperture was chosen to minimize the contribution of the impact cloud to the lightcurve. A rotational period of (40.832 ± 0.33) h (A'Hearn et al., 2005) was assumed, while zero rotational phase was set to the time of impact. In Fig. 5, the CN flux within the integration area is shown, normalized to the mean value of all data points. The different colors indicate data points from different slit orientations. The error bars in rotational period arise from the uncertainty in the nucleus rotation period. Data points with the same slit orientation show a smooth variation with rotational phase. Differences between the data points from different slit orientations are caused by coma asymmetry. The coma asymmetry becomes larger at large rotational phases. A correlation of the inner coma brightness with rotational phase can be seen, with an increased brightness between rotational phases of 0.1 and 0.25, and a second maximum around phase values of 0.65. The data obtained in the night July 05/06 do not properly fit into the rotational lightcurve. This could be caused either by an underestimated photometric error, or by a significant contribution of the impact cloud. The night July 05/06 is the only night with non-photometric conditions in the observing campaign described. The photometric uncertainty was estimated from the deviation of observed standard star spectra from their catalogue spectra. But it cannot be ruled out that the sky conditions were different at the time of the comet observations, causing the error to be underestimated. Furthermore, the small field of view used for the determination of the lightcurve should exclude the major part of the impact cloud, nevertheless, one cannot exclude a small remaining contribution of the order of a few percent.

In Fig. 6, the normalized fluxes originating from the radicals CN, C_2, C_3, and NH_2 are shown, including observations from all position angles. Different colors correspond to the fluxes of the emissions from the four different species. The correlation of

Table 7
The ratios between the production rates before and after impact and the number of molecules in the impact cloud, given for the different position angles

Ratio	p.a.	Before impact	Impact cloud	After impact
C_2/CN	0°	1.60 ± 0.27	1.12 ± 0.21	1.16 ± 0.25
	90°	1.73 ± 0.28	2.05 ± 0.74	1.72 ± 0.37
	180°	1.55 ± 0.33	1.06 ± 0.21	1.44 ± 0.20
	270°	1.34 ± 0.47	1.93 ± 0.61	0.98 ± 0.04
	Mean	1.56 ± 0.16	1.54 ± 0.52	1.33 ± 0.32
C_3/CN	0°	0.17 ± 0.05	0.29 ± 0.06	0.17 ± 0.01
	90°	0.19 ± 0.06	0.08 ± 0.02	0.18 ± 0.01
	180°	0.13 ± 0.01	0.16 ± 0.07	0.08 ± 0.03
	270°	0.12 ± 0.01	0.17 ± 0.03	0.12 ± 0.01
	Mean	0.15 ± 0.03	0.18 ± 0.09	0.14 ± 0.05

Note. The row marked with "mean" gives the value averaged from all four position angles.

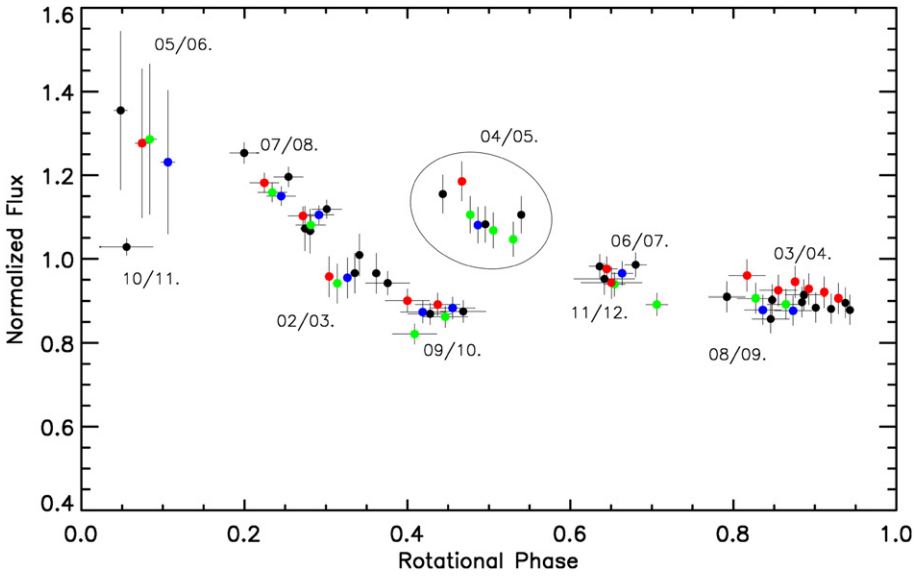

Fig. 5. The normalized rotational CN lightcurve. Different position angles are indicated by colors: black—0°–180°, red—90°–270°, blue—45°–225°, green—135°–315°. (For interpretation of the references to color in this figure legend, the reader is referred to the web version of this article.)

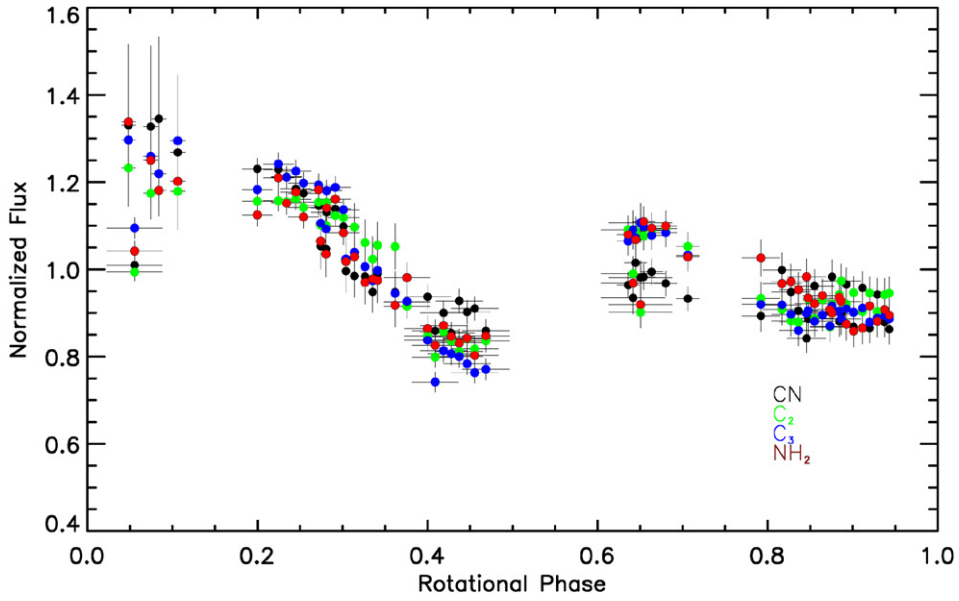

Fig. 6. The normalized rotational lightcurve for the species CN, C_2, C_3, and NH_2, given in different colors. All slit orientations are shown. The night of July 04/05, following the impact, is excluded in this figure. (For interpretation of the references to color in this figure legend, the reader is referred to the web version of this article.)

the inner coma brightness with rotational phase can be seen for all four species.

The different species included in Fig. 6 show the same behavior with rotation, with the exception of CN at rotational phases around 0.65. Here, the brightness of the CN line emission in the night of July 06/07 (the data points with the smaller error bars in rotational phase in Fig. 6) clearly is below the normalized brightness of all other species. In the night of July 11/12, at similar rotational phase, the CN data point and the data point for C_3 are in good agreement with the data from July 06/07. The C_2 and NH_2 data points of that night show no significant difference from the CN value. It remains unclear whether the observations on July 11/12 reflect a change in the physical properties of the cometary coma, or if they are caused by uncertainties in data calibration. Since no correction for possible straylight in frames taken with FORS1 was possible (Rauer et al., 2006), an additional source of uncertainty remains in the FORS1 observations from July 10/11 and 11/12, compared to the other observations done with FORS2. At the edges of the slit of FORS1, where the comet signal is lowest, remnant features in the comet frames after sky subtraction were found, showing differences between both edges of the slit. This improper sky subtraction is more significant at larger wavelengths, while a relatively good sky subtraction was achieved at wavelengths less than about 4300 Å. Therefore, it cannot be ruled out that the observations of C_2 and NH_2 with FORS1 are affected by calibration uncertainties that cannot be quantified.

8. Summary and discussion

The analysis of the radial emission profiles originating from CN, C_2, C_3, and NH_2 in nights around the Deep Impact event lead to the following results:

- After the Deep Impact event at Comet 9P/Tempel 1, a gas cloud expanding in the coma was observed. A mean expansion velocity of (1.23 ± 0.12) km s^{-1} for CN and (1.17 ± 0.14) km s^{-1} for C_2 was measured for the outermost part of the cloud. Velocities of (0.63 ± 0.04) km s^{-1} and (0.75 ± 0.04) km s^{-1} were measured for the center of the CN and C_2 clouds, respectively.
- Based on the Haser-like chemistry model, a total number of parent molecules produced by the impact event of $(3.48 \pm 0.87) \times 10^{29}$ for the CN parent, $(5.20 \pm 1.48) \times 10^{29}$ molecules for the C_2 parent, and $(0.66 \pm 0.48) \times 10^{29}$ molecules for the C_3 parent were determined.
- The abundance of C_2 and C_3 relative to CN in the impact cloud is in agreement with the pre-impact coma composition. No signs of compositional differences between the material sublimating from the surface or near-surface of the nucleus and the impact material which was possibly ejected from deeper surface layers was found from the study of the CN, C_2, and C_3 parent species.
- The production rates of CN, C_2, C_3, and NH_2 as measured five and six nights after the impact are in agreement with the pre-impact production rates.
- A variation of the gas production of all four species studied with the rotation of the nucleus was detected. A primary maximum at a rotational phase of about 0.2 and a secondary maximum at a rotational phase of 0.65 can be identified. These maxima can be explained by the presence of active surface areas on the comet nucleus, moving in and out of sunlight as the nucleus rotates.
- The rotational variation of all species are in agreement except at a rotational phase of 0.6 to 0.7. In this phase range, the brightness of the CN emission is significantly lower than the emissions from C_2, C_3, and NH_2 in the night of

July 06/07. Additional observations at similar rotational phase on July 11/12 are not conclusive.

If the observed variation in activity with rotational phase of the nucleus is caused by located active areas on the nucleus surface, the disagreement of the CN lightcurve with the lightcurves for the other species at rotational phases around 0.65 could possibly indicate a compositional difference between the different parts of the nucleus surface. The active area causing the secondary maximum in the lightcurve than would have a lower content of the CN parent compared to the rest of the comets nucleus. HCN is a likely parent species for CN, although for comets at heliocentric distances less than 3 AU also additional sources of CN may be of importance (Fray et al., 2005). Indications on compositional differences between different parts of the surface of Comet Tempel 1 were discussed before. Feaga et al. (2006) report of an asymmetry of the CO_2 and H_2O distribution in the inner coma of Comet Tempel 1, derived from infrared spectra from the Deep Impact flyby spacecraft. Therefore, even if no compositional difference between the usual activity of Comet Tempel 1 and the material from deeper layers ejected by the impact could be found, indications for compositional variations between different parts of the cometary surface were obtained.

Acknowledgments

The authors wish to thank E. Jehin and O. Hainaut for their support of the observations on which this work is based on. C. Sterken acknowledges financial support from the Belgian Fund for Scientific Research (FWO).

References

A'Hearn, M.F., Millis, R.L., Schleicher, D.G., Osip, D.J., Birch, P.V., 1995. The ensemble properties of comets: Results from narrowband photometry of 85 comets, 1976–1992. Icarus 118, 223–270.

A'Hearn, M.F., and 32 colleagues, 2005. Deep Impact: Excavating Comet Tempel 1. Science 310, 258–264.

Cochran, A.L., Barker, E.S., Ramseyer, T.F., Storrs, A.D., 1992. The McDonald Observatory Faint Comet Survey—Gas production is 17 comets. Icarus 98, 151–162.

Feaga, L.M., A'Hearn, M.F., Sunshine, J.M., Groussin, O., and the Deep Impact Science Team, 2006. Asymmetry of gaseous CO_2 and H_2O in the inner coma of Comet Tempel 1. Lunar Planet. Sci. XXXVII. Abstract 2149.

Fink, U., Combi, M.R., Disanti, M.A., 1991. Comet P/Halley—Spatial distributions and scale lengths for C_2, CN, NH_2, and H_2O. Astrophys. J. 383, 356–371.

Fray, N., Benilan, Y., Cottin, H., Gazeau, M.-C., Crovisier, J., 2005. The origin of the CN radical in comets: A review from observations and models. Planet. Space Sci. 53, 1243–1262.

Huebner, W.F., Keady, J.J., Lyon, S.P., 1992. Solar photo rates for planetary atmospheres and atmospheric pollutants. Astrophys. Space Sci. 195, 1–289, 291–294.

Kawakita, H., Watanabe, J., 2002. Revised fluorescence efficiencies of cometary NH_2: Ammonia abundances is comets. Astrophys. J. 572, L177–L180.

Meech, K.J., and 208 colleagues, 2005. Deep Impact: Observations from a worldwide Earth-based campaign. Science 310, 265–269.

Rauer, H., and 12 colleagues, 2003. Long-term optical spectrophotometric monitoring of Comet C/1995 O1 (Hale–Bopp). Astron. Astrophys. 397, 1109–1122.

Rauer, H., Weiler, M., Sterken, C., Jehin, E., Knollenberg, J., Hainaut, O., 2006. Observations of CN and dust activity of comet 9P/Tempel 1 around Deep Impact. Astron. Astrophys. 459, 257–263.

Schleicher, D.G., 1983. The fluorescence of cometary OH and CN. Ph.D. thesis, University of Maryland.